Geophysical Research Letters

Key Points:
- First statistical wave normal analysis on very low frequency (VLF) transmitter signals in the magnetosphere is presented
- Dominance of nonducted signals is revealed in the magnetosphere
- The power proportions of ducted and nonducted signals are given as a function of L and Kp index

Correspondence to:

W. Gu and L. Chen,
wxg170330@utdallas.edu;
lunjin.chen@gmail.com

Direct Evidence Reveals Transmitter Signal Propagation in the Magnetosphere

Wenyao Gu[1], Lunjin Chen[1], Zhiyang Xia[1], and Richard B. Horne[2]

[1]Physics Department, W. B. Hanson Center for Space Sciences, University of Texas at Dallas, Richardson, TX, USA, [2]British Antarctic Survey, Cambridge, UK

Abstract Signals from very-low-frequency transmitters on the ground are known to induce energetic electron precipitation from the Earth's radiation belts. The effectiveness of this mechanism depends on the propagation characteristics of those signals in the magnetosphere, and in particular whether the signals are ducted or nonducted along channels of enhanced plasma density, analogous to optical fibers. Here we perform a statistical analysis of in-situ waveform data collected by the Van Allen Probes satellites that shows that nonducted propagation dominates over ducted propagation in both the occurrence and intensity of the waves. Ray tracing confirms that the latitudinal distribution of wavevectors corresponds to nonducted as opposed to ducted propagation. Our results show the dominant mode of propagation needed to quantify transmitter-induced precipitation and improve the forecast of electron radiation belt dynamics for the safe operation of satellites.

Plain Language Summary Very Low Frequency (VLF) signals emitted from ground-based transmitters can appear in the Earth's magnetosphere, propagating either in ducted mode along magnetic lines or in nonducted mode. The different propagation modes affect how the signals interact with energetic electrons of the radiation belts and precipitate them into the ionosphere. In this study, we present a statistical study using the observations of Alpha transmitter signals by Van Allen Probes satellites and show that nonducted propagation mode dominates over ducted propagation mode in both signal occurrence and wave intensity. Our result is also supported by ray-tracing simulations. Our study not only resolves the relative contribution of different propagation modes, but also provides critical parameters for quantifying precipitation by VLF transmitter signals and therefore improving forecast of radiation belt electron dynamics.

1. Introduction

Powerful ground-based very low frequency (VLF) transmitters, which operate at tens of kHz with power ranging from several 100 s to 1,000 kW (Volakis, 2007; Watt, 1967), have been utilized for maintaining long distance communication with submarines for decades dating back to the era before World War II (Sterling, 2007). The long-distance communication is realized by radio wave propagation in the ionosphere-Earth waveguide (Wait, 1957). A fraction of the radio wave power can leak through the ionosphere into the magnetosphere (Maeda & Oya, 1963), where VLF signals propagate in the whistler-mode (Helliwell, 1965; Leiphart et al., 1962). There are two modes of propagation for VLF transmitter signals in the inner magnetosphere: ducted and nonducted. Ducted waves propagate inside a density enhancement or depletion known as a duct, with wave energy and wave normal direction confined nearly along the ambient field lines (Cerisier, 1974; Helliwell, 1965; Sonwalkar & Inan, 1986). Both observations (Moullard et al., 2002; Scarf & Chappell, 1973; Sonwalkar et al., 1994) and modeling (Katoh, 2014; Ke et al., 2021) reveal that wave power can be modulated and focused by density ducts with various spatial scales, even with spatial scales comparable or smaller than signal wavelength (Hosseini et al., 2021; Streltsov et al., 2006; Zudin et al., 2019). Ducted propagation mode has been assumed for numerous theoretical studies on wave-particle interaction (Gołkowski et al., 2019). Nonducted waves propagate in a spatially smoothly varying medium, with wave normal gradually refracted away from the Earth and approaching oblique resonance cone angles (Cerisier, 1973). Both waves are capable of precipitating energetic electrons below 2 MeV in the inner belt and slot region (corresponding to L = 1–3, mainly inside the plasmasphere) by scattering them into the drift loss cone (Abel & Thorne, 1998; Agapitov et al., 2014; Albert et al., 2020; Gamble et al., 2008; Hua et al., 2020; Inan et al., 2007; Kulkarni et al., 2008; Ma et al., 2017; Rodger et al., 2010; Ross et al., 2019). Ducted waves

are more efficient at scattering <800 keV electrons (Abel & Thorne, 1998; Gamble et al., 2008; Rodger et al., 2010; Ross et al., 2019), primarily through first-order cyclotron resonance (Rodger et al., 2010), while nonducted waves allow Landau resonance and cyclotron resonances at higher equatorial pitch angles (Abel & Thorne, 1998; Ross et al., 2019). Understanding of VLF transmitter signals' propagation is critical for addressing their roles in electron precipitations in the inner magnetosphere (Albert et al., 2020; Ross et al., 2019; Starks et al., 2020).

Despite general recognition that signals from transmitters propagate mainly in nonducted mode at L < 1.5 (Agapitov et al., 2014; Cerisier, 1973; Clilverd et al., 2008; Gamble et al., 2008; Ma et al., 2017; Rodger et al., 2010; Zhang et al., 2018), there is still under great debate over how the signals propagate throughout the inner magnetosphere (Agapitov et al., 2014; Bell et al., 1981; Clilverd et al., 2008; Inan et al., 1977; Ma et al., 2017; Zhang et al., 2018). Earlier works use indirect evidence based on signal time delay analysis and suggest more frequent nonducted signals than ducted (Bell et al., 1981; Inan et al., 1977). In recent decades, statistical studies on wave intensities suggest majorly ducted propagations at 1.7 < L < 2.5 (Clilverd et al., 2008; Ma et al., 2017), based on comparison with the half electron gyrofrequency cut-off of ducted signals (Smith, 1961). A consistency between wave intensity distribution and ray tracing results on the meridional plane supports the domination of nonducted signals in the magnetosphere (Zhang et al., 2018). The increased occurrence of nonducted waves in disturbed periods (Kp > 3) are suggested indirectly by electrostatic features at higher latitudes (Agapitov et al., 2014).

One main reason for the inconsistencies among the conclusions from different studies is the lack of direct statistical evidence, which also results in an inability to quantify the relative contribution of either propagation mode. The spatial distribution of wave intensity may not be sufficient to differentiate the two propagation modes, since, like nonducted waves, ducted waves can spread over a range of L values because of the finite area of transmitter signal intensity illuminated in the topside ionosphere (Starks et al., 2020; Zhang et al., 2018). A unique feature that is, capable of directly differentiating propagation modes is in-situ wave normal direction measurement near the equatorial magnetosphere, where signal propagation takes place. With the recently decommissioned Van Allen Probes satellites (2012–2019), bursts of electromagnetic waveforms are collected by the Electric and Magnetic Field Instrument Suite and Integrated Science (EM-FISIS) instrument at a sufficient sampling rate (35 kHz) over a span of ~7 years over magnetic latitudes of −20°–10° (Kletzing et al., 2013) and thus wave normal analysis becomes available for VLF transmitters with frequencies below 12 kHz (due to instrumental attenuation above it). Fortunately, there exists powerful ground VLF transmitters that operate below this frequency limit. The transmitters of the Russian Alpha radio navigation system (RSDN-20) emit signal pulses at frequency F1 = 11.9 kHz and with power 500 kW. The system consists of three main transmitters over L-shells of L = 1.8–2.7 (Koronczay et al., 2018): Krasnodar (45.4°N, 38.1°E), Novosibirsk (55.8°N, 84.4°E), and Khabarovsk (El'ban) (50.1°N, 136.6°E) (Zhang et al., 2017). In this paper, we present the first statistical study on in-situ wave normal analysis of these transmitter signals to resolve the dispute over propagation modes.

2. Methodology

2.1. Indentification of Alpha Transmitter Signals

According to Alpha signals' intensity peaks at topside ionosphere (Vavilov et al., 2013; Zhang et al., 2017) (illustrated in Supporting Information Figure S1 by DEMETER observations (Parrot et al., 2006)), the Alpha signals are confined within northern magnetic foot points locating within a magnetic latitude range of 30°–80° and a magnetic longitude range of 80°–240°. Continuous burst waveform observations of Van Allen Probes within this foot point region are used for the analysis. Probe A covers the period from September 2012 to December 2017 and Probe B covers the period from September 2012 to May 2018.

The three orthogonal magnetic and electric field components are measured in the spinning coordinates (named UVW) (Wygant et al., 2013), for each burst of duration 6 s. For each 6 s waveform, we used shifted-window fast Fourier transform with a time window of 0.03 s and a time shift of 0.015 s to obtain the magnetic/electric power spectral density in U, V, and W axes. The frequency channel width of each waveform is 34.2 Hz. Total magnetic (electric) power spectral density was obtained from the sum of the corresponding three components.
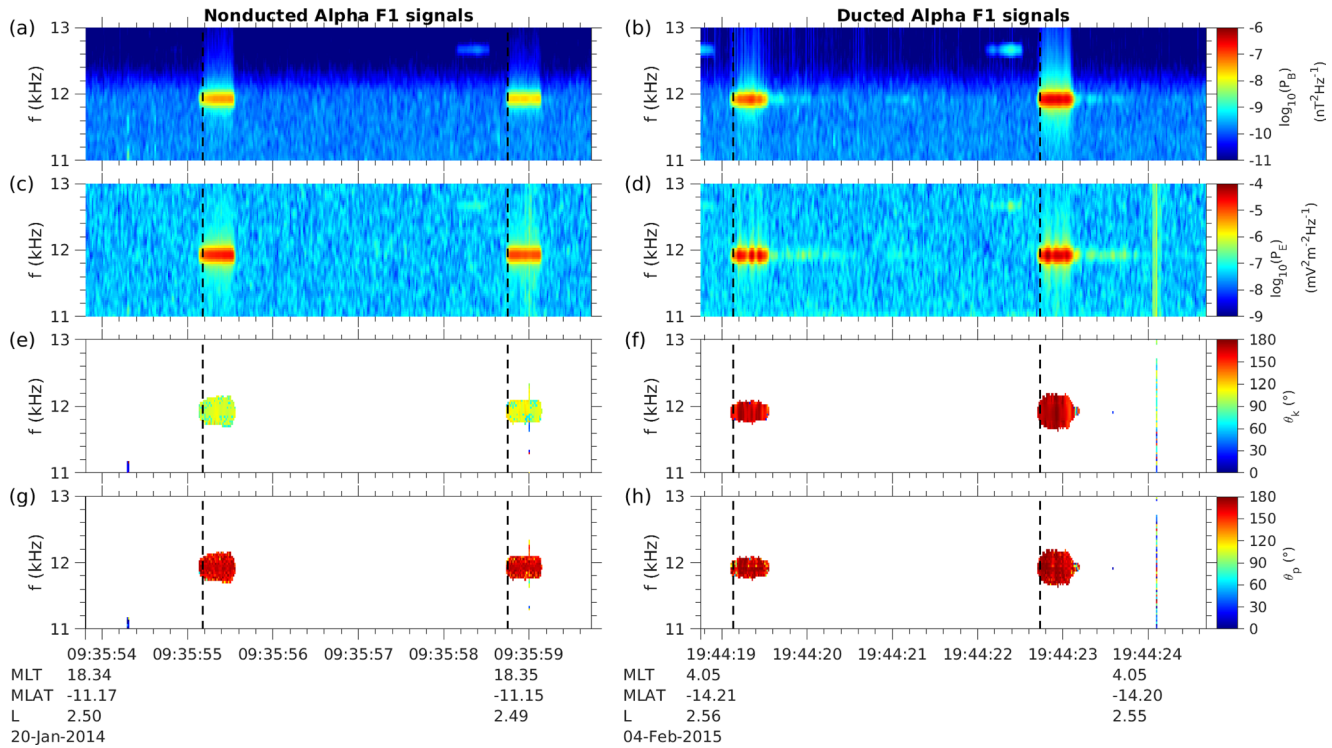
Figure 1. Examples of nonducted (left) and ducted (right) signals from Van Allen Probe A. (a) and (b) Magnetic field power spectral density. The vertical black dashed lines denote the identified F1 signal starting times. The pattern of repetitive 0.4 s pulses every 3.6 s can be seen. (c) and (d) Electric field power spectral density. (e) and (f) Polar angle of wave normal k vector. (g)–(h) Polar angle of Poynting vector. The polar angles are defined with respect to the background magnetic field with 0° (180°) denoting parallel (antiparallel) directions.

The Alpha transmitter signals were identified automatically based on recognizable pulse patterns at frequency F1 = 11.9 kHz with a fixed duration of 0.4 s and a fixed repetition period of 3.6 s (Koronczay et al., 2018). Figure 1 shows two examples of the identified Alpha transmitter signals with magnetic power spectrum (Figures 1a and 1b) and electric power spectrum (Figures 1c and 1d). Two identification criteria are both required for either the total magnetic or electric power spectral density obtained above. The first criterion below ensures that there exists a peak of the power spectral density at frequency F1:

$$P(F1) - max(P(F1^+), P(F1^-)) > 0.25P(F1) \tag{1}$$

where $P(\mathrm{F1})$, $P(\mathrm{F1}^+)$, and $P(\mathrm{F1}^-)$ are running mean of power spectral density with a running time window of 0.4 s for the frequency channel at, just above, and just below F1 = 11.9 kHz, respectively. The second criterion is to identify 0.4 s pulse intervals whose mean power spectral density at F1 bin exceeds both that 0.2 s just before and after. Those identified intervals that are close within 0.4 s were grouped and their medium interval was selected as an identified pulse interval. Additional manual inspection was performed to remove any false identification.

2.2. Waveform Analysis

For each identified transmitter pulse of 0.4 s, the median magnetic amplitude B and electric amplitude E (Kletzing et al., 2013) were calculated using the spectral power density over three frequency bins in the vicinity of F1 frequency, corresponding to a bandwidth of ~100 Hz. Poynting P vectors, wavenumber k vectors, planarity, and ellipticity were obtained by the SVD method of 6-channel orthogonal electromagnetic fields (Santolík et al., 2003), and their medium values over the 0.4 s pulse duration were recorded for each pulse. For Poynting P and wavenumber k vectors, we calculated the medium values of three orthogonal components of their unit vectors in field-aligned coordinates, which are used to identify the directions of the "medium" vectors of the identified pulses. Signals with extremely small amplitudes (satisfying both
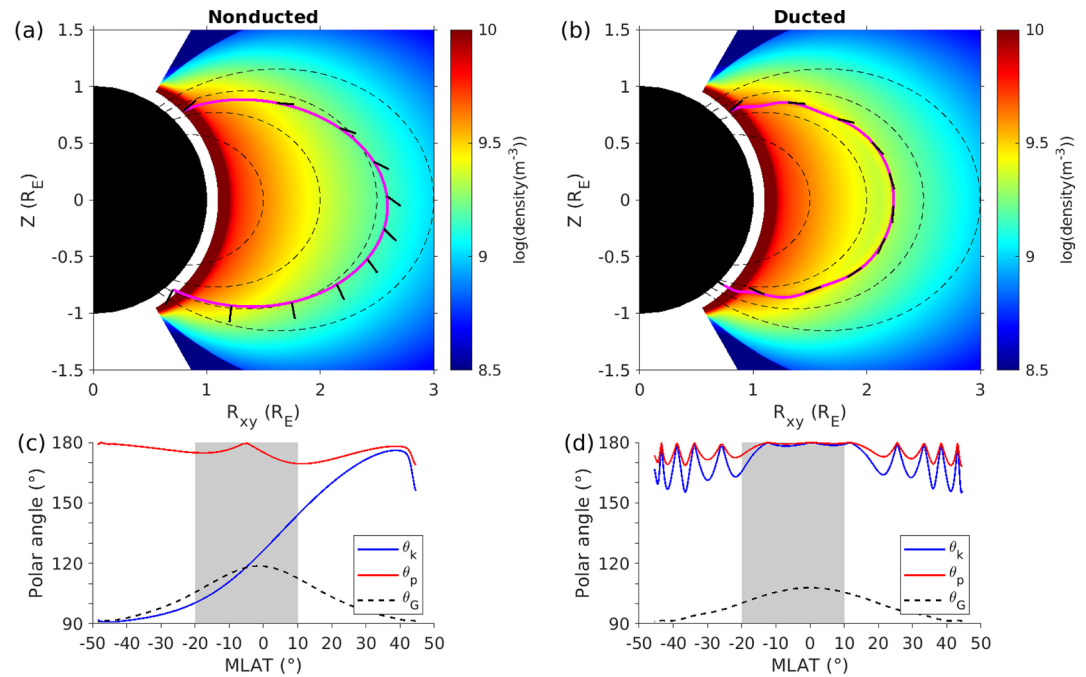
Figure 2. Ray-tracing comparisons between nonducted (a), (c) and ducted (b), (d) propagation modes. The rays are launched at the position of the intensity peak of the NOV station in Figure S1b at 700 km altitude with initial wave normal along the transmission cone. The background density distribution, typical for nightside (Bortnik et al., 2011), is color-coded and the magenta lines show ray paths. The black short line segments denote wave normal directions. Dipole magnetic field is used in ray tracing. The dashed lines in (a) and (b) denotes field lines with L values of 1.5, 2.0, 2.5, and 3.0. For the nonducted (c) and ducted (d) rays, the polar angles of k vector and Poynting vector are plotted in the blue and red lines correspondingly. The black dashed lines in (c) and (d) denote the Gendrin angle. The gray patched area shows the magnetic latitude coverage of Van Allen Probes observations.

$B < 10^{-3.75}$ nT and $E < 10^{-2.75}$ mV/m) were excluded. We also excluded signals with median planarity at F1 frequency bin smaller than 0.75. In total, 52,475 signals were identified.

3. Propagation of Alpha Signals in the Magnetosphere

Two examples of the Van Allen Probes waveform measurements with each lasting 6 s, one for nonducted and the other for ducted Alpha transmitter signals, are shown in Figure 1. Those signals have an identifiable pattern of repetitive pulses with a fixed duration of 0.4 s every 3.6 s. The two examples show a distinct wave normal angle θ_k which is highly oblique (~110°) and characteristic of nonducted propagation (Figure 1e), and the other nearly field-aligned (~160°) and characteristic of ducted propagation (Figure 1f). The polar angle θ_p of the Poynting vector with respect to the background magnetic field line is similarly close to the anti-parallel direction (>150°) for both modes (Figures 1g and 1h). The density duct corresponding to the ducted signals in Figure 1 is shown in Supporting Information Figure S2 (Kurth et al., 2015).

Ray tracing simulation of nonducted and ducted propagation was done by the HOTRAY code (Horne, 1989) using a general nightside background electron density profile (Bortnik et al., 2011) with and without a density crest, respectively. Both rays were launched from the northern hemisphere and the ray tracing results are depicted in Figure 2. For ducted propagation (Figure 2b), a Gaussian density duct of 20% density enhancement and 0.05 L-shell width is added at L = 2.2, which agrees with the typical duct parameters inside the plasmasphere (Scarf & Chappell, 1973; Sonwalkar, 2006). As a result of the field line curvature, the wave normal of the nonducted ray gradually refracts radially outwards during southward propagation and reaches 100°–140° over the latitudinal range (−20°–10°) of Van Allen Probes (Figures 2a and 2c). In contrast, the wave normal of the ducted ray oscillates around and keeps aligned with the field line (Figures 2b and 2d). The smallness of the inclination between the Poynting vector and the field line for both rays (Figures 2c and 2d) is consistent with the observations shown in Figures 1g and 1h. The nonducted ray at
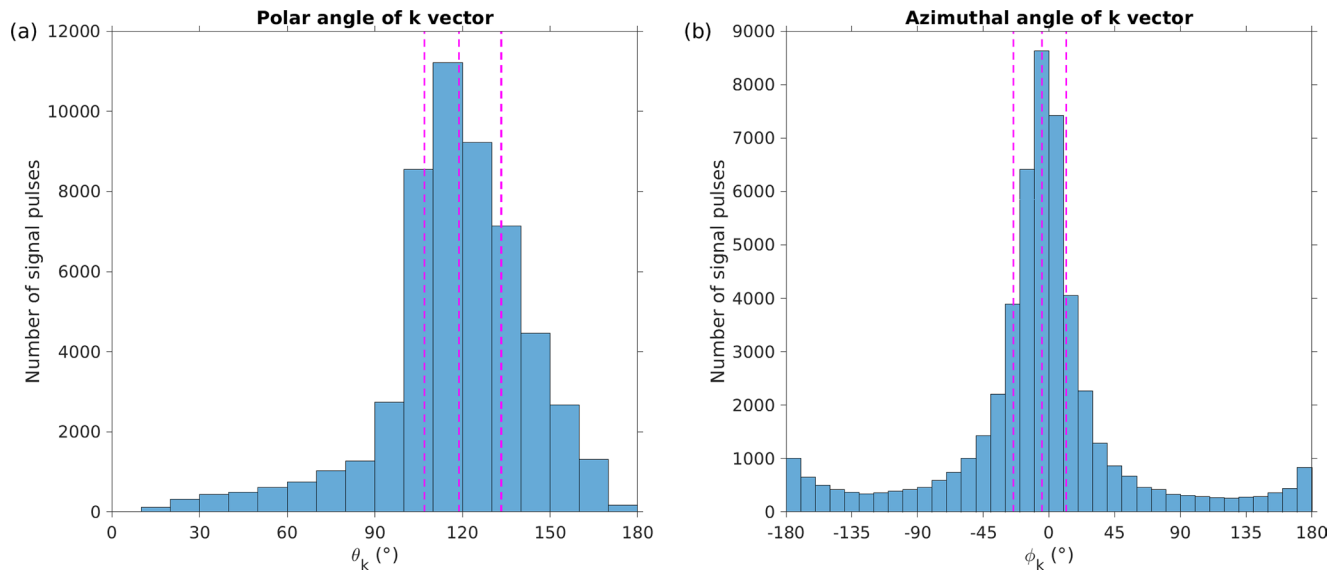
Figure 3. Histograms of signal occurrence as a function of wave normal (a) polar angles and (b) azimuthal angles. The 25%, 50%, and 75% quantiles are shown in magenta dashed lines. Azimuthal angle of 0° (180°) denotes radially outward (inward) direction, and that of 90° (−90°) denotes eastward (westward) direction. For the azimuthal angle histogram (b), signal pulses with medium wave normal polar angle <20° or >160° are excluded.

first propagates to higher L-shell along with increasing wave normal angles, but then moves back to lower L-shell (Zhang et al., 2018) with an inward Poynting vector after the wave normal angle goes beyond the Gendrin angle (Figure 2a). Consequently, the nonducted ray may reach close to the transmitter's conjugate point as the ducted ray does, and the comparison between the illuminated areas in the two hemispheres is not sufficient to differentiate between the two modes.

4. Statistical Waveform Analysis

In total 52,745 signal pulses from Alpha transmitters were identified by the twin Van Allen Probes (A and B) from September 2012 to May 2018. Similar to the two examples shown in Figure 1, propagation properties of each pulse were analyzed by the SVD technique using six-orthogonal components of magnetic and electric fields. Medium values of wavenumber k and Poynting p vectors over the pulse duration of 0.4 s were extracted for every pulse. The direction of both vectors is expressed in terms of polar angles (θ_k, θ_p) and azimuthal angles (ϕ_k, ϕ_p), defined with respect to the background magnetic field. θ_k coincides with the definition of wave normal angle. Those angles were used for statistical analysis below to obtain relative contribution of different propagation modes.

Figure 3 shows the normalized occurrences of θ_k and ϕ_k. Since azimuthal angles, ϕ_k, lose their meaning for propagation parallel to the Earth's magnetic field (and anti-parallel), the occurrences with θ_k smaller than 20° or greater than 160° were excluded in the azimuthal angle histogram (Figure 3b). One can see a pronounced peak occurrence of wave normal direction with southward propagation at oblique polar angles (∼110°) and pointing radially outward ($\phi_k \sim 0°$), both of which are signatures of propagation characteristics of nonducted propagation (Figure 2a), supporting the dominance of nonducted propagation. To put a lower limit of relative nonducted occurrence, we found 69% of the pulse wavenumbers having polar angles in the θ_k range of 100°–140° (Figures 3a) and 64% having radially outward direction in the ϕ_k range of −30°–30° (Figure 3b). In contrast, only 3% (12%) of the pulses have polar angles above 160° (above 145°), which is the signature of ducted propagation. One can also note that a small fraction of occurrences exhibit northward propagation (i.e., reflected from the southern hemisphere), with θ_k below 90°. Since those reflected pulses have most occurrences near the perpendicular direction ($\theta_k = 90°$), we used the polar angle of Poynting vector θ_p instead of the wave vector to identify the reflected signal occurrence and found 7.5% of occurrences for reflected signals with $\theta_p > 0°$ (corresponding to the northward propagation).
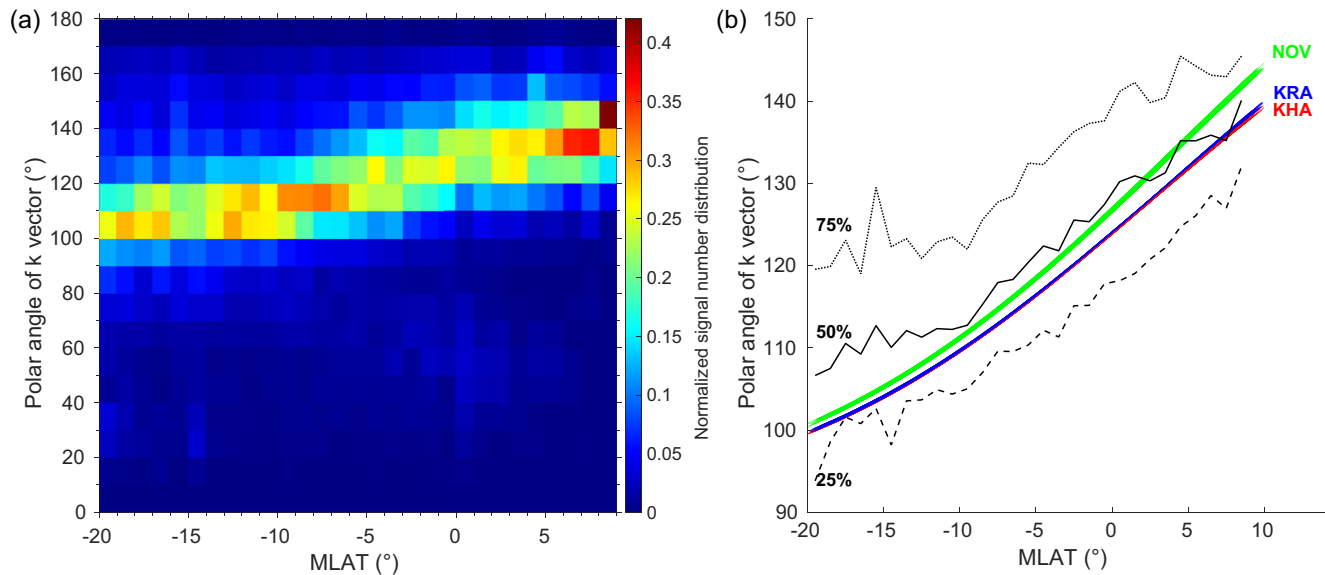
Figure 4. Relation between the wavenumber polar angles and magnetic latitudes. (a) Normalized signal occurrence distribution with MLAT and wave normal polar angles. The latitudinal bin size = 1° and the normalization is done within each bin. (b) The ray tracing wave normal angles from three stations are shown in red (KHA), green (NOV), and blue (KRA) lines. The background magnetic field is dipole. The background density is set as the typical night side values (Bortnik et al., 2011). For each station, a set of 36 rays are launched from the edges of the transmission cone uniformly. The rays start at the maximum intensity peak for each station in Figure S1 at 700 km altitude. Quantiles of the signal number occurrence distribution as functions of wave normal angles at different MLAT bins are shown in dashed black (25%), solid black (50%), and dotted black (75%) lines for comparison.

Another distinct feature between ducted and nonducted propagation is the variation of wave normal angle θ_k with magnetic latitude (Figure 2). During southward propagation, the wave normal angle of the nonducted ray tends to decrease and approaches 90° (Figure 2a) while that of the ducted ray tends to oscillate near 180° and does not exhibit a monotonic variation with magnetic latitude (Figure 2b). Figure 4a shows the normalized occurrence of Alpha signal pulses detected by Van Allen Probes in θ_k bins (of bin width 10°) with normalization done for every bin (1°) of magnetic latitude. The observed θ_k concentrates around an oblique angle above 90° for all latitudes. As the latitude decreases from 10° to −20°, θ_k decreases monotonically from ~140° to ~105° and approaches 90°, which provides further evidence of the dominance of nonducted propagation over ducted propagation. Moreover, we also performed ray tracing simulation for nonducted propagation. A set of 36 rays from each of the three Alpha stations (the locations corresponding to the peak intensity at 700 km altitude in Supporting Information Figure S1) were launched with initial wavenumber vectors spanning over the transmission cone, whose size was calculated by a typical nighttime E layer electron density of 5×10^4 cm^{-3} (Zhang et al., 2018). The variations of simulated and observed θ_k as a function of magnetic latitudes are compared in Figure 4b. One can see that the ray tracing results follow the same monotonic trend in latitude as the observations and lie closely with the 50th percentile of the occurrence rate and within the 25th–75th percentiles. The results definitively support that the latitudinal distribution of wave vectors corresponds to nonducted as opposed to ducted propagation.

To quantify the relative contribution of ducted and nonducted signals, we examined a pool (27,623) of the pulses with southward propagation and observed over MLAT < −5°, and used a critical wave normal angle θ_{kc} of 145° to separate ducted ($\theta_k > \theta_{kc}$) from nonducted ($\theta_k < \theta_{kc}$) propagation. The choice of the latitudinal range and the critical θ_{kc} allows for the optimal separation (with justification provided in Supporting Information), as nonducted θ_k deviates further from ducted θ_k (near 180°) as the latitude decreases (Figures 2c and 2d). In total, 2631 (~10%) out of the pool were identified as ducted signals. Figure 5a shows occurrence rates of ducted signals as a function of L. The occurrence rates here are the ratios of ducted pulse number to the total pulse number inside each L-bin of bin width 0.2. For L < 3 where the pulse occurrence number is sufficient, the occurrence rate of ducted signals is 6%–14%, which is consistent with the analysis above that most signals are nonducted and also with other indirect analysis (Agapitov et al., 2014; Bell et al., 1981; Cerisier, 1973; Inan et al., 1977; Zhang et al., 2018). The ducted occurrence rate increases with L value.
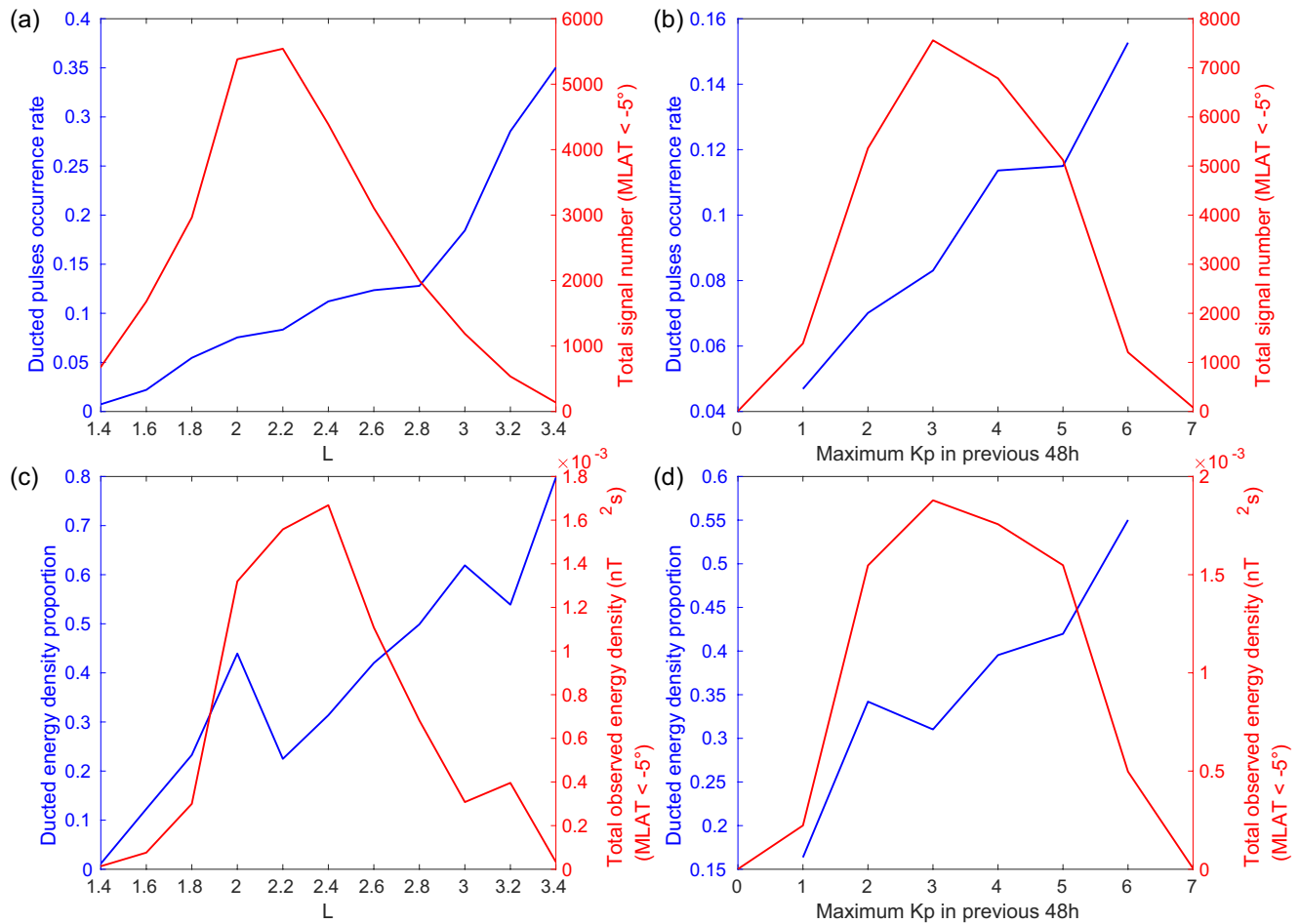
Figure 5. Statistical results on ducted pulses occurrence rate and ducted power. The ducted pulse occurrence rate here denotes the fraction of pulses that are ducted and the ducted energy density proportion denotes the fraction of the total measured energy density that is due to ducted pulses. (a) The red line shows total southward propagating signal numbers per 0.2 L-shell. The samples are confined to southward propagating signals observed at MLAT < −5°. Southward propagation requires both parallel components of k vectors and of Poynting vectors pointing southward. The blue line indicates the occurrence rate of ducted signals with wave normal angles larger than θkc = 145°. (b) Same as (a) but with x-axis in every 1 bin of maximum Kp index in the previous 48 h of each observation. (c) The red line shows the total observed propagating signal power per 0.2 L-shell with the same sample pool as (a). The blue line indicates the power proportion of ducted signals. (d) Same as (c) but with x-axis in every 1 bin of maximum Kp index in the previous 48 h of each observation.

There could be two potential reasons for this L-dependence. First, nearly vertically aligned field lines in the ionosphere at higher L are favorable for guiding signals from the transmission cone in ducts (Clilverd et al., 2008). Therefore, ducted propagation at lower L requires higher density crest enhancement (Clilverd & Horne, 1996; Ross et al., 2019), which is less frequent. Second, frequent and large density irregularities are often found just inside and near the plasmapause (LeDocq et al., 1994; Darrouzet et al., 2004). Figure 5b shows that the occurrence rates of ducted signals increase with the maximum Kp index in the past 48 h of the observation. The result is consistent with previous results based on indirect ground-based observation (Thomson et al., 1997). During higher geomagnetic activity, the plasmapause is eroded inwards (Carpenter & Anderson, 1992; Moldwin et al., 2002) and the occurrence probability of density irregularities near the plasmapause is enhanced (Darrouzet et al., 2004), which could lead to an increase in ducted propagation.

Few Alpha signals (141 signals) are observed beyond L = 3.4. For ducted signals, the cut-off at half equatorial electron gyrofrequency (Smith, 1961) is located at L ∼ 3.3. For nonducted signals, ray-tracing results with a range of initial magnetic latitudes covering the illumination area at DEMETER shows that the F1 frequency signals near the equator are confined within L ∼ 3.0 (shown in Supporting Information Figure S3 (Shklyar et al., 2010)). Therefore, neither ducted nor nonducted signals are likely to reach beyond L = 3.4.

Although less frequent, the observed ducted signals often have higher intensities than the nonducted signals (Figure 1). Here we provide an estimation of relative contribution of ducted signals to the overall intensity, which is of direct relevance to the capability of transmitter waves in scattering energetic electrons in the radiation belts. For the pool of transmitter signals, the magnetic power spectral density within 100 Hz of F1 frequency was used to obtain the wave intensity. The intensity of ducted signals is 33% of total intensity. This percentage is obtained as the ratio of the sum of wave magnetic energy density of ducted pulses to that of all pulses in the examined pool. Figure 5c shows the relative contribution of ducted intensity as a function of L, with a significant increase from L = 1.5 (∼0%) to L = 3.4 (∼80%). Figure 5d illustrates its relationship with the maximum Kp index of the past 48 h. Similar to the occurrence rate, the intensity contribution also increases remarkably from ∼15% during geomagnetic quiet times to ∼50% during active times.

For the wave normal angle distribution of transmitter signals, one would expect two distinct peaks, one for nonducted signals and the other for ducted signals. However, the in-situ measurement shows the prevalence of nonducted propagation, and does not show a peak associated with ducted signals in Figure 3a, due to a small occurrence rate of ducted signals. Nonetheless, two peaks can be discerned in the distribution of wave intensity, with a peak at $\theta_k \sim 115°$ for the nonducted signals and another peak at $\theta_k \sim 170°$ for the ducted signals (shown in Supporting Information Figure S4). Such a two-peak structure appears because ducted signals on average carry more intensity than nonducted signals.

5. Discussions

The study focuses on the Alpha transmitter signals at 11.9 kHz, which are emitted over a mid-latitude range from MLAT = 30° to MLAT = 50° (Supporting Information Figure S1), and are observed near the equatorial region from L ∼ 1.4 to L ∼ 3.4 (Figure 5). The majority of ground-based transmitters, however, cover a relatively broad frequency range of 18–28 kHz and are located at a relatively wide range of magnetic latitudes (21°–57°) (Meredith et al., 2019). The three transmitters NWC (19.9 kHz, MLAT = −31.0°), NAA (24.0 kHz, MLAT = 53.8°), and DHO38 (23.4 kHz, MLAT = 53.5°) account for 50% of the total transmitter power in 1.3 < L < 3.0 (Meredith et al., 2019). For these transmitters' signals emitted from the mid-latitudes, we expect similar propagation physics to the Alpha transmitter signals, and thus expect a trend of propagation modes with L-shell and geomagnetic conditions similar to the observations in Figure 5. For signals observed at L < 1.5 from lower-latitude stations (NWC and NPM), most of them are also suggested to be in the nonducted mode (Clilverd et al., 2008; Gamble et al., 2008; Ma et al., 2017; Rodger et al., 2010). The dominant nonducted mode revealed in our study using wave normal directions is consistent with the statistic results using wave power distribution (Zhang et al., 2018).

The proportion of ducted pulse occurrence and ducted energy density is related to prevalence of field-aligned density irregularities inside the plasmasphere (Thomas et al., 2021). These density irregularities can also serve as ducts for natural occurring VLF waves, such as lightening-generated whistlers (Angerami, 1970) and hiss (Koons, 1989). Therefore, a further understanding of these density structure is necessary for building up the picture of VLF wave propagation in the plasmasphere.

6. Conclusions

Analysis of in-situ waveform measurement of ground transmitter signals near the equatorial magnetosphere reveals wave polarization characteristics and relative contribution of ducted and nonducted signals to occurrence and wave intensity. These results provide the information required to quantify electron loss from the radiation belts due to VLF transmitter signals which up to now has had to be assumed and has been the subject of much uncertainty. The following points are listed for conclusion:

1. A statistical study on magnetospheric propagations of Alpha transmitter signals is presented based on the 7 years observation of Van Allen Probes. The statistical results of wave vector distributions and their variation across latitudes, together with ray-tracing evidence, unambiguously support the dominant occurrence of nonducted signals.
2. The sum of wave energy density of ducted signals takes up 33% of the total energy density.
3. Both the occurrence rate and the wave intensity proportion of ducted signals increase with higher L-shells and higher maximum Kp index in the previous 48 h.

Data Availability Statement

Data and codes used for Figures 2–5 and Figure S4 are provided in https://doi.org/10.5281/zenodo.4985773.

References

Abel, B., & Thorne, R. M. (1998). Electron scattering loss in earth's inner magnetosphere: 2. Sensitivity to model parameters. *Journal of Geophysical Research*, *103*(A2), 2397–2407. https://doi.org/10.1029/97JA02920

Agapitov, O. V., Artemyev, A. V., Mourenas, D., Kasahara, Y., & Krasnoselskikh, V. (2014). Inner belt and slot region electron lifetimes and energization rates based on akebono statistics of whistler waves. *Journal of Geophysical Research: Space Physics*, *119*(4), 2876–2893. https://doi.org/10.1002/2014JA019886

Albert, J. M., Starks, M. J., Selesnick, R. S., Ling, A. G., O'Malley, S., & Quinn, R. A. (2020). Vlf transmitters and lightning-generated whistlers: 2. Diffusion of radiation belt electrons. *Journal of Geophysical Research: Space Physics*, *125*(3), e2019JA027030. https://doi.org/10.1029/2019JA027030

Angerami, J. J. (1970). Whistler duct properties deduced from vlf observations made with the ogo 3 satellite near the magnetic equator. *Journal of Geophysical Research*, *75*(31), 6115–6135. https://doi.org/10.1029/JA075i031p06115

Bell, T. F., Inan, U. S., & Helliwell, R. A. (1981). Nonducted coherent vlf waves and associated triggered emissions observed on the isee-1 satellite. *Journal of Geophysical Research*, *86*(A6), 4649–4670. https://doi.org/10.1029/JA086iA06p04649

Bortnik, J., Chen, L., Li, W., Thorne, R. M., & Horne, R. B. (2011). Modeling the evolution of chorus waves into plasmaspheric hiss. *Journal of Geophysical Research*, *116*(A8), A08221. https://doi.org/10.1029/2011JA016499

Carpenter, D. L., & Anderson, R. R. (1992). An isee/whistler model of equatorial electron density in the magnetosphere. *Journal of Geophysical Research*, *97*(A2), 1097–1108. https://doi.org/10.1029/91JA01548

Cerisier, J. (1973). A theoretical and experimental study of non-ducted vlf waves after propagation through the magnetosphere. *Journal of Atmospheric and Terrestrial Physics*, *35*(1), 77–94. https://doi.org/10.1016/0021-9169(73)90217-1

Cerisier, J. (1974). Ducted and partly ducted propagation of vlf waves through the magnetosphere. *Journal of Atmospheric and Terrestrial Physics*, *36*(9), 1443–1467. https://doi.org/10.1016/0021-9169(74)90224-4

Clilverd, M. A., & Horne, R. B. (1996). Ground-based evidence of latitude-dependent cyclotron absorption of whistler mode signals originating from vlf transmitters. *Journal of Geophysical Research*, *101*(A2), 2355–2367. https://doi.org/10.1029/95JA03153

Clilverd, M. A., Rodger, C. J., Gamble, R., Meredith, N. P., Parrot, M., Berthelier, J.-J., & Thomson, N. R. (2008). Ground-based transmitter signals observed from space: Ducted or nonducted? *Journal of Geophysical Research*, *113*(A4), A04211. https://doi.org/10.1029/2007JA012602

Darrouzet, F., Décréau, P. M. E., De Keyser, J., Masson, A., Gallagher, D. L., Santolik, O., et al. (2004). Density structures inside the plasmasphere: Cluster observations. *Annales Geophysicae*, *22*(7), 2577–2585. https://doi.org/10.5194/angeo-22-2577-2004

Gamble, R. J., Rodger, C. J., Clilverd, M. A., Sauvaud, J.-A., Thomson, N. R., Stewart, S. L., et al. (2008). Radiation belt electron precipitation by man-made VLF transmissions. *Journal of Geophysical Research*, *113*(A10), A10211. https://doi.org/10.1029/2008JA013369

Gołkowski, M., Harid, V., & Hosseini, P. (2019). Review of controlled excitation of non-linear wave-particle interactions in the magnetosphere. *Frontiers in Astronomy and Space Sciences*, *6*, 2. https://doi.org/10.3389/fspas.2019.00002

Helliwell, R. A. (1965). *Whistlers and related ionospheric phenomena*. Stanford University Press.

Horne, R. B. (1989). Path-integrated growth of electrostatic waves: The generation of terrestrial myriametric radiation. *Journal of Geophysical Research*, *94*(A7), 8895–8909. https://doi.org/10.1029/JA094iA07p08895

Hosseini, P., Agapitov, O., Harid, V., & Gołkowski, M. (2021). Evidence of small scale plasma irregularity effects on whistler mode chorus propagation. *Geophysical Research Letters*, *48*(5), e2021GL092850. https://doi.org/10.1029/2021GL092850

Hua, M., Li, W., Ni, B., Ma, Q., Green, A., Shen, X., et al. (2020). Very-low-frequency transmitters bifurcate energetic electron belt in near-earth space. *Nature Communications*, *11*, 4847. https://doi.org/10.1038/s41467-020-18545-y

Inan, U. S., Bell, T. F., Carpenter, D. L., & Anderson, R. R. (1977). Explorer 45 and imp 6 observations in the magnetosphere of injected waves from the siple station vlf transmitter. *Journal of Geophysical Research*, *82*(7), 1177–1187. https://doi.org/10.1029/JA082i007p01177

Inan, U. S., Golkowski, M., Casey, M. K., Moore, R. C., Peter, W., Kulkarni, P., et al. (2007). Subionospheric vlf observations of transmitter-induced precipitation of inner radiation belt electrons. *Geophysical Research Letters*, *34*(2), L02106. https://doi.org/10.1029/2006GL028494

Katoh, Y. (2014). A simulation study of the propagation of whistler-mode chorus in the earth's inner magnetosphere. *Earth Planets and Space*, *66*, 6. https://doi.org/10.1186/1880-5981-66-6

Ke, Y., Chen, L., Gao, X., Lu, Q., Wang, X., Chen, R., et al. (2021). Whistler-mode waves trapped by density irregularities in the earth's magnetosphere. *Geophysical Research Letters*, *48*(7), e2020GL092305. https://doi.org/10.1029/2020GL092305

Kletzing, C. A., Kurth, W. S., Acuna, M., MacDowall, R. J., Torbert, R. B., Averkamp, T., et al. (2013). The electric and magnetic field instrument suite and integrated science (emfisis) on rbsp. *Space Science Reviews*, *179*(1), 127–181. https://doi.org/10.1007/s11214-013-9993-6

Koons, H. C. (1989). Observations of large-amplitude, whistler mode wave ducts in the outer plasmasphere. *Journal of Geophysical Research*, *94*(A11), 15393–15397. https://doi.org/10.1029/JA094iA11p15393

Koronczay, D., Lichtenberger, J., Juhász, L., Steinbach, P., & Hospodarsky, G. (2018). VLF transmitters as tools for monitoring the plasmasphere. *Journal of Geophysical Research: Space Physics*, *123*(11), 9312–9324. https://doi.org/10.1029/2018JA025802

Kulkarni, P., Inan, U. S., Bell, T. F., & Bortnik, J. (2008). Precipitation signatures of ground-based VLF transmitters. *Journal of Geophysical Research*, *113*(A7), A07214. https://doi.org/10.1029/2007JA012569

Kurth, W. S., De Pascuale, S., Faden, J. B., Kletzing, C. A., Hospodarsky, G. B., Thaller, S., & Wygant, J. R. (2015). Electron densities inferred from plasma wave spectra obtained by the waves instrument on van allen probes. *Journal of Geophysical Research: Space Physics*, *120*(2), 904–914. https://doi.org/10.1002/2014JA020857

LeDocq, M. J., Gurnett, D. A., & Anderson, R. R. (1994). Electron number density fluctuations near the plasmapause observed by the crres spacecraft. *Journal of Geophysical Research*, *99*(A12), 23661–23671. https://doi.org/10.1029/94JA02294

Leiphart, J. P., Zeek, R. W., Bearce, L. S., & Toth, E. (1962). Penetration of the ionosphere by very-low-frequency radio signals-interim results of the lofti i experiment. *Proceedings of the IRE*, *50*(1), 6–17. https://doi.org/10.1109/JRPROC.1962.288269

Ma, Q., Mourenas, D., Li, W., Artemyev, A., & Thorne, R. M. (2017). VLF waves from ground-based transmitters observed by the van allen probes: Statistical model and effects on plasmaspheric electrons. *Geophysical Research Letters*, *44*(13), 6483–6491. https://doi.org/10.1002/2017GL073885

Maeda, K., & Oya, H. (1963). Penetration of VLF radio waves through the ionosphere. *Journal of Geomagnetism and Geoelectricity*, *14*(3), 151–171. https://doi.org/10.5636/jgg.14.151

Meredith, N. P., Horne, R. B., Clilverd, M. A., & Ross, J. P. J. (2019). An investigation of VLF transmitter wave power in the inner radiation belt and slot region. *Journal of Geophysical Research: Space Physics*, *124*(7), 5246–5259. https://doi.org/10.1029/2019JA026715

Moldwin, M. B., Downward, L., Rassoul, H. K., Amin, R., & Anderson, R. R. (2002). A new model of the location of the plasmapause: CRRES results. *Journal of Geophysical Research*, *107*(A11), 1339. https://doi.org/10.1029/2001JA009211

Moullard, O., Masson, A., Laakso, H., Parrot, M., Décréau, P., Santolik, O., & Andre, M. (2002). Density modulated whistler mode emissions observed near the plasmapause. *Geophysical Research Letters*, *29*(20), 361–364. https://doi.org/10.1029/2002GL015101

Parrot, M., Benoist, D., Berthelier, J., Blecki, J., Chapuis, Y., Colin, F., et al. (2006). The magnetic field experiment imsc and its data processing onboard demeter: Scientific objectives, description and first results. *Planetary and Space Science*, *54*(5), 441–455. https://doi.org/10.1016/j.pss.2005.10.015

Rodger, C. J., Carson, B. R., Cummer, S. A., Gamble, R. J., Clilverd, M. A., Green, J. C., et al. (2010). Contrasting the efficiency of radiation belt losses caused by ducted and nonducted whistler-mode waves from ground-based transmitters. *Journal of Geophysical Research*, *115*(A12), A12208. https://doi.org/10.1029/2010JA015880

Ross, J. P. J., Meredith, N. P., Glauert, S. A., Horne, R. B., & Clilverd, M. A. (2019). Effects of VLF transmitter waves on the inner belt and slot region. *Journal of Geophysical Research: Space Physics*, *124*(7), 5260–5277. https://doi.org/10.1029/2019JA026716

Santolík, O., Parrot, M., & Lefeuvre, F. (2003). Singular value decomposition methods for wave propagation analysis. *Radio Science*, *38*(1), 1010. https://doi.org/10.1029/2000RS002523

Scarf, F. L., & Chappell, C. R. (1973). An association of magnetospheric whistler dispersion characteristics with changes in local plasma density. *Journal of Geophysical Research*, *78*(10), 1597–1602. https://doi.org/10.1029/JA078i010p01597

Shklyar, D. R., Parrot, M., Chum, J., Santolik, O., & Titova, E. E. (2010). On the origin of lower- and upper-frequency cutoffs on wedge-like spectrograms observed by demeter in the midlatitude ionosphere. *Journal of Geophysical Research*, *115*(A5), A05203. https://doi.org/10.1029/2009JA014672

Smith, R. L. (1961). Propagation characteristics of whistlers trapped in field-aligned columns of enhanced ionization. *Journal of Geophysical Research*, *66*(11), 3699–3707. https://doi.org/10.1029/JZ066i011p03699

Sonwalkar, V. S. (2006). The influence of plasma density irregularities on whistler-mode wave propagation. In J. W. LaBelle & R. A. Treumann (Eds.), *Geospace electromagnetic waves and radiation* (pp. 141–190). Berlin, Heidelberg: Springer. https://doi.org/10.1007/3-540-33203-0_6

Sonwalkar, V. S., & Inan, U. S. (1986). Measurements of siple transmitter signals on the de 1 satellite: Wave normal direction and antenna effective length. *Journal of Geophysical Research*, *91*(A1), 154–164. https://doi.org/10.1029/JA091iA01p00154

Sonwalkar, V. S., Inan, U. S., Bell, T. F., Helliwell, R. A., Chmyrev, V. M., Sobolev, Y. P., et al. (1994). Simultaneous observations of VLF ground transmitter signals on the de 1 and cosmos 1809 satellites: Detection of a magnetospheric caustic and a duct. *Journal of Geophysical Research*, *99*(A9), 17511–17522. https://doi.org/10.1029/94JA00866

Starks, M. J., Albert, J. M., Ling, A. G., O'Malley, S., & Quinn, R. A. (2020). VLF transmitters and lightning-generated whistlers: 1. Modeling waves from source to space. *Journal of Geophysical Research: Space Physics*, *125*(3), e2019JA027029. https://doi.org/10.1029/2019JA027029

Sterling, C. H. (2007). *Military communications: From ancient times to the 21st century*. ABC-CLIO.

Streltsov, A. V., Lampe, M., Manheimer, W., Ganguli, G., & Joyce, G. (2006). Whistler propagation in inhomogeneous plasma. *Journal of Geophysical Research*, *111*(A3), A03216. https://doi.org/10.1029/2005JA011357

Thomas, N., Shiokawa, K., Miyoshi, Y., Kasahara, Y., Shinohara, I., Kumamoto, A., et al. (2021). Investigation of small-scale electron density irregularities observed by the arase and van allen probes satellites inside and outside the plasmasphere. *Journal of Geophysical Research: Space Physics*, *126*(3), e2020JA027917. https://doi.org/10.1029/2020JA027917

Thomson, N. R., Clilverd, M. A., & Smith, A. J. (1997). Evidence of more efficient whistler-mode transmission during periods of increased magnetic activity. *Annales Geophysicae*, *15*(8), 999–1004. https://doi.org/10.1007/s00585-997-0999-9

Vavilov, D., Shklyar, D., Titova, E., & Parrot, M. (2013). Study of the lower hybrid resonance frequency over the regions of gathering earthquakes using demeter data. *Journal of Atmospheric and Solar-Terrestrial Physics*, *100–101*, 1–12. https://doi.org/10.1016/j.jastp.2013.03.019

Volakis, J. L. (2007). *Antenna engineering handbook*. McGraw-Hill.

Wait, J. R. (1957). The mode theory of VLF ionospheric propagation for finite ground conductivity. *Proceedings of the IRE*, *45*(6), 760–767. https://doi.org/10.1109/JRPROC.1957.278469

Watt, A. D. (1967). *VLF radio engineering*. Pergamon Press.

Wygant, J., Bonnell, J., Goetz, K., Ergun, R., Mozer, F., Bale, S., et al. (2013). The electric field and waves instruments on the radiation belt storm probes mission. *Space Science Reviews*, *179*(1–4), 183–220. https://doi.org/10.1007/s11214-013-0013-7

Zhang, X., Zhao, S. F., Ruzhin, Y., Liu, J., & Song, R. (2017). The spatial distribution features of three alpha transmitter signals at the topside ionosphere. *Radio Science*, *52*(5), 653–662. https://doi.org/10.1002/2016RS006219

Zhang, Z., Chen, L., Li, X., Xia, Z., Heelis, R. A., & Horne, R. B. (2018). Observed propagation route of vlf transmitter signals in the magnetosphere. *Journal of Geophysical Research: Space Physics*, *123*(7), 5528–5537. https://doi.org/10.1029/2018JA025637

Zudin, I. Y., Zaboronkova, T. M., Gushchin, M. E., Aidakina, N. A., Korobkov, S. V., & Krafft, C. (2019). Whistler waves' propagation in plasmas with systems of small-scale density irregularities: Numerical simulations and theory. *Journal of Geophysical Research: Space Physics*, *124*(6), 4739–4760. https://doi.org/10.1029/2019JA026637